Solar Physics (2021) 296:115
https://doi.org/10.1007/s11207-021-01856-8

Relating 27-Day Averages of Solar, Interplanetary Medium Parameters, and Geomagnetic Activity Proxies in Solar Cycle 24

Yvelice Castillo[1,2,3] · Maria Alexandra Pais[2,3] · João Fernandes[2,4] · Paulo Ribeiro[2] · Anna L. Morozova[2] · Fernando J.G. Pinheiro[2]

Received: 22 October 2020 / Accepted: 22 June 2021

Abstract
Correlations between solar, interplanetary-medium parameters, and geomagnetic-activity proxies in 27-day averages (a Bartels rotation) were analyzed for the 2009 – 2016 time interval. In this analysis, two new proxies were considered: i) B_{zs} GSM (Geocentric Solar Magnetic), calculated as the daily percentage of the IMF southward component along the GSM z-axis and then averaged every 27 days; ii) four magnetospheric indices (T-indices), calculated from the local north–south (x) contributions of the magnetosphere's cross-tail (TAIL), the symmetric ring current (SRC), the partial ring current (PRC), and the Birkeland current (FAC), derived from the Tsyganenko and Sitnov (*J. Geophys. Res.* **110**, A03208, 2005: TS05) semi-empirical magnetospheric model. Our results suggest that, among the parameters tested in this study, solar facular areas, interplanetary magnetic-field intensity and new proxies derived from the TS05 model could be taken into account in an empirical model, with a 27-day resolution, to explain geomagnetic activity felt on the Earth's surface in terms of solar-surface features and the IMF condition. We further retrieve a clear annual oscillation in series of 27-day-mean values of toward/away asymmetries of geomagnetic-activity indices, which can be interpreted in the light of the Russell–McPherron hypothesis for the semiannual variation of geomagnetic activity.

Keywords Solar active regions · Solar wind disturbances · Magnetosphere · Geomagnetic disturbances

1. Overview

Space weather (SWE) concerns the impact on the Heliosphere of variable conditions on the Sun. This includes the electromagnetic perturbations due to solar and cosmic-ray fluxes in the near-Earth environment and their effects in the technological and biological systems. The Sun and its activity are the sources of energy in the causal chain of processes of SWE. The most energetic solar events, such as white light flares and coronal mass ejections (CMEs), can drastically alter the level of electromagnetic and corpuscular radiation of the interplanetary medium with consequent disturbance of the equilibrium state of the terrestrial magnetosphere–ionosphere coupled system, causing geomagnetic storms that can

Extended author information available on the last page of the article

Published online: 27 July 2021

damage navigation and communication systems and power lines. SWE affects our modern way of life, sometimes in drastic ways. Its potential impact is growing as we become more dependent on technological systems (Schrijver, 2015). The severity of the effects on almost all technologies depends in part on the geomagnetic latitude, being particularly important for the higher latitudes and for the South Atlantic Anomaly (Thomson, 2013). Mid-latitudes are also significantly perturbed by geomagnetic storms. These adverse effects include the loss of HF communications, damage in high-voltage power supply lines or pipelines, and deterioration of services provided by global navigation satellite systems (e.g. Buonsanto, 1999; Beggan et al., 2013). A deeper understanding of SWE events can be used to forecast hazards and to define strategies for mitigating their impact. Interest in, and dependence on, SWE information and services grows rapidly, due to its importance for technological infrastructures, impact on global economy, and growing need for SWE hazards mitigation (Schrijver, 2015).

The comparison between solar parameters, parameters of the solar wind, and geomagnetic-activity indices is of particular interest for identification of causal relationships between solar and terrestrial phenomena. The main goal of this study is to identify those solar, interplanetary medium, and geomagnetic-activity parameters that show the strongest statistical relations, and to sort out the best candidates to relate meaningfully solar activity to geomagnetic disturbances felt on Earth's surface. We use widely known proxies, such as the Sun's northern and southern facular areas (FA-N and FA-S), total and southward components of the interplanetary magnetic field [B and B_z, respectively], and Newell's coupling function (NLL), and we test two new types of parameters. The first new parameter is the daily percentage of the southward component of the interplanetary magnetic field (IMF) in the Geocentric Solar Magnetospheric (GSM) coordinate system, which we call B_{zs}. Another group of new proposed parameters consists in indices derived from simulations, using the TS05 (Tsyganenko and Sitnov, 2005) magnetospheric semi-empirical model of the geomagnetic-field variations near the ground at middle latitudes, which we call T-indices.

1.1. Solar Hemispherical Asymmetry

Solar magnetic activity is controlled by differential rotation and meridional circulation in both hemispheres, but it manifests itself differently in each one. Waldmeier (1971) found that the Sun's hemispheric asymmetry extends to different aspects of magnetic activity. During recent years the asymmetries in variations of many solar parameters have been confirmed by several authors: for the sunspot number and areas (Ballester, Oliver, and Carbonell, 2005; Temmer et al., 2006), facular region areas (Gonçalves et al., 2014), X-ray flares flux (Joshi et al., 2015), velocity of torsional oscillations (Lekshmi, Nandy, and Antia, 2018), and for the temporal delay on the reversal time polarity of the north and south solar magnetic field (Janardhan et al., 2018). It was also shown that those asymmetries might have an impact on the Earth's climate (Georgieva et al., 2007). A phase lag of activity between the northern and southern solar hemispheres typically ranges from one day to a year or two (Dorotovič et al., 2010). This suggests that the coupling between the two hemispheres is variable and weak (Norton and Gallagher, 2009). The north–south asymmetry of sunspot activity results in asynchronous reversal of the Sun's polar field and may affect the strength of the solar cycle. It appears that cycles with strong asymmetry tend to have a lower amplitude (e.g. Cycles 23 and 24) in comparison with cycles in which sunspot activity in the two hemispheres is more synchronized (e.g. Cycles 21 and 22) (Mordvinov et al., 2016). On the other hand, the causes of the asymmetry are under debate. Several authors point out a connection between the asymmetry and the solar dynamo (see Schüssler and Cameron, 2018; Nepomnyashchikh et al., 2019 and the references therein). It seems that the combination of dipolar

mode and quadrupolar modes, with periods of about 22 years and between 13 and 15 years, respectively, can reproduce the observed patterns of the north and south asymmetry. The study of the hemispheric asymmetry has become a valuable tool to evaluate solar-activity properties and in development of dynamo theories. For example, in the recent work of Perri et al. (2018), the simulations of the solar wind, coupling solar-dynamo and solar-wind models, showed the clear impact of the hemispheric asymmetry on the solar-wind properties (velocity and magnetic fields).

Here, we consider the effect of solar hemispherical asymmetries of sunspot numbers (e.g. Temmer, Veronig, and Hanslmeier, 2002) using data from SILSO (Royal Observatory of Belgium, Brussels) and of the facular areas computed from images taken at the spectroheliograph of the Geophysical and Astronomical Observatory of the University of Coimbra (OGAUC). The hypothesis that these asymmetries might constrain the geomagnetic activity on Earth is tested.

1.2. Simulations of Magnetospheric Contributions

Castillo et al. (2017) tested the TS05 model against measurements at the Earth's surface, and they showed it to be a useful tool to help in understanding the observations of the x-component of geomagnetic activity. For the four mid-latitude stations considered in that study, and using in the analysis all geomagnetically active days during the eight-year period from 2007 to 2014, around 50 % of observed daily series were reproduced by the TS05 model with correlation coefficients above 0.7. TS05 model estimates are computed using near-Earth satellite measurements of the solar-wind plasma and the interplanetary magnetic field (e.g. Tsyganenko and Sitnov, 2005; Tsyganenko and Andreeva, 2015) from NASA/Goddard Space Flight Center's OMNI data through OMNIWeb (omniweb.gsfc.nasa.gov/form/omni_min.html). Input data comprise: the interplanetary magnetic field (IMF) components (B_x GSM, B_y GSM, B_z GSM), the flow-speed components (V_x GSE, V_y GSE, V_z GSE), the solar-wind ram pressure, proton density and proton temperature, the SYM-H index, and the Earth's geomagnetic-dipole tilt angle. Semi-empirical relations between the magnetospheric and solar-wind/IMF parameters are used to compute the magnetic-field vectors associated with five magnetospheric-current systems: i) the symmetrical ring current (SRC); ii) the asymmetrical, or partial ring current (PRC); iii) the cross-tail sheet current (TAIL); iv) a system of two vertical currents called field-aligned currents or Birkeland currents (FAC), that connect ionosphere and magnetosphere in the polar regions; and v) a current flowing in the magnetospheric boundary called the magnetopause current or the Chapman–Ferraro current (CF).

Since, in the TS05 model, the inner ring current and the more distant tail current sheet form a current system circulating close and parallel to the geomagnetic equator, the variability associated to these currents is more clearly retrieved in the x-component of the geomagnetic field (Castillo et al., 2017). We computed estimates of hourly values for the x-component at the four northern hemisphere mid-latitude geomagnetic observatories of Coimbra (Portugal), Panagurishte (Bulgary), Novosibirsk (Russia), and Boulder (USA) (see Castillo et al., 2017), for the period 2009 – 2016, keeping separate contributions from different sources. Table 1 shows the geographic and geomagnetic coordinates of the four observatories. Geomagnetic coordinates were computed using the IGRF-12 model for 2010.0. The y-component variability, being strongly dependent on the FAC current system because of its poloidal symmetry, is expected to be significantly affected by the unrealistic closure of FAC through the Earth's center in the TS05 model. Statistical results reported by Castillo et al. (2017) confirmed that the TS05 model performs better in reproducing the x-

Table 1 Stations and their geographic and geomagnetic coordinates.

Station	Geographic Coord.		Geomagnetic Coord.	
	Lat. [°N]	Long. [°E]	Lat. [°N]	Long. [°E]
COI	40.2	351.6	43.8	72.1
PAG	42.5	24.2	40.5	105.1
NVS	54.9	83.2	45.4	156.0
BOU	40.1	254.8	48.1	321.3

than the y-variability. For this reason, only TS05 simulations for the x-component were used to compute the T-indices.

The article is organized as follows: Section 1 gives background for the present study. Section 2 presents the analyzed parameters and the methods used to calculate them. Section 3 presents results of the correlation analysis and discusses them. The main conclusions are drawn in Section 4.

2. Data

All parameters analyzed in this study were averaged over the Bartels period of solar rotation (i.e. a 27-day time interval), in order to filter out the recurrence tendency of geomagnetic activity associated with the distinct influence of different solar sectors. Temporal averaging over a Bartels rotation period allows us to estimate the mean influence that the Sun may have on the Earth, taking into account the effect of all solar longitudes. Parameters are listed in Table 2 together with their source databases. The analyzed temporal interval covers an abnormally long period of weak solar activity with a minimum of the total solar irradiance in 2009, and both the rising and part of the declining phases of Solar Cycle 24. This solar cycle is particularly interesting due to the triple polarity reversal in the Sun's Northern Hemisphere, its smaller amplitude with respect to previous cycles and the long duration of its minimum (Mordvinov et al., 2016; Janardhan et al., 2018). Some of the analyzed series are shown in Figures 1 – 4 as a function of Bartels rotation number.

In order to perform a cross-correlation analysis, we grouped the parameters into five sets: solar parameters (SP), parameters of the solar wind (SWP), IMF components (IMF), geomagnetic activity indices (GAI), and indices obtained from TS05's simulations, or T-indices (TI).

2.1. Solar Parameters (SP)

Most of the solar parameters analyzed here refer to features at the solar photosphere and chromosphere: the international northern/southern hemisphere's sunspot number (SN-N/SN-S), the international total sunspot number (SN-T), the difference between northern and southern sunspot numbers (SN-NS), the northern/southern hemisphere's facular area (FA-N/FA-S), the difference between northern and southern facular areas (FA-NS) – see Figure 1. The sunspot numbers are obtained from the Sunspot Index and Long-term Solar Observations (SILSO) database at the Royal Observatory of Belgium. The facular areas were calculated by Barata et al. (2018), using the computational tool developed by them. The 27-day-averaged data is shown at Figure 1. We also used the solar radio flux at 10.7 cm wavelength ($F_{10.7}$), originating in the chromosphere and corona of the Sun.

Table 2 33 parameters analyzed and their data sources, separated by SP, SWP, IMF, GAI, and TI. Explanations in the text.

No.	Solar Parameters (SP)	Source
1	FA-T, total facular area [% of solar disk].	Calculated by Barata et al. (2018).
2	FA-N, Northern facular area [% of solar disk].	
3	FA-S, Southern facular area [% of solar disk].	
4	SN-T, total international sunspot number.	WDC-SILSO, Royal Observatory of Belgium, Brussels.
5	SN-N, Northern hemisphere's sunspot number.	
6	SN-S, Southern hemisphere's sunspot number.	
7	FA-NS, FA-N minus FA-S [%].	Obtained from items (2) and (3).
8	SN-NS, SN-N minus SN-S.	Obtained from items (5) and (6).
9	$F_{10.7}$, solar radio flux of 10.7 cm [sfu].	NASA/GSFC's OMNI daily data (King and Papitashvili, 2005 and omniweb.gsfc.nasa.gov/form/dx1.html).
	Solar Wind (SWP) and IMF parameters	
10 – 13	T: proton temperature [10^3 K], ρ: proton density [N cm^{-3}], V: bulk flow speed [km s^{-1}], p: flow pressure [nPa].	NASA/GSFC's OMNI daily data.
14 – 16	B_x, B_y GSE, and B_z GSE [nT].	NASA/GSFC's OMNI daily data.
17 – 18	B_y GSM, and B_z GSM [nT].	
19	B: magnitude of average field vector [nT].	
	Geomagnetic activity indices (GAI)	
20	Newell's coupling function, NLL	Tsyganenko's yearly data files for TA15 model. Tsyganenko's 5-min Newell's data can be downloaded at geo.phys.spbu.ru/~tsyganenko/TA_2016_RBF.
21 – 27	Kp10, AE, AU, AL, PCN [mV m^{-1}], Dst [nT], Ap [nT] indices	NASA/GSFC's OMNI daily data.
	New indices	
28 – 29	B_{zs} GSE and B_{zs} GSM.	Calculated by us with NASA/GSFC's OMNI hourly data.
30 – 33	T-TAIL, T-SRC, T-PRC, and T-FAC indices [nT].	Calculated by us from their respective TS05 sources. For more details see Castillo et al. (2017).

2.2. Solar Wind (SWP) and IMF Parameters

Solar-wind parameters are the solar-wind bulk speed in km s^{-1} [V], proton flux temperature in Kelvin [T], proton density in N cm^{-3} [ρ], where N is the number of protons, and solar-wind proton ram pressure in nPa [p], measured by spacecraft at the outer magnetosphere.

The IMF parameters are the components of the interplanetary magnetic field B_x, B_y, B_z, in nT, in two different reference frames, both having the x-axis pointing away from the Earth toward the Sun: the GSM and the Geocentric Solar Ecliptic (GSE). While GSM has the y-

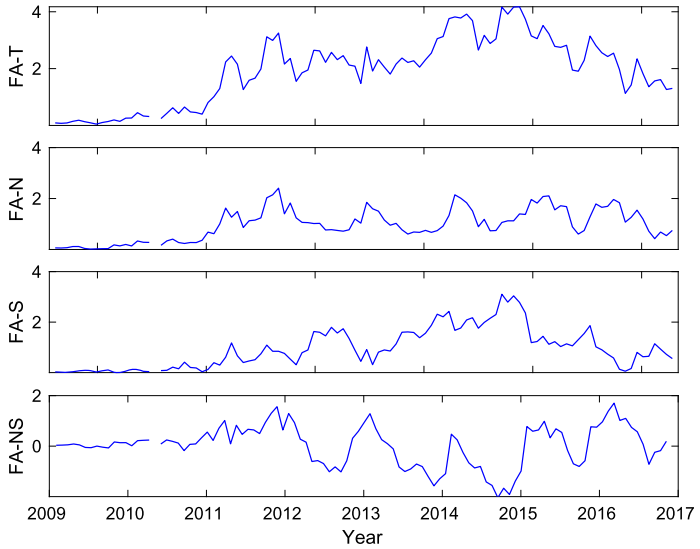

Figure 1 Time series of 27-day-averaged facular areas, in percentage of total solar disk area. From top to bottom: the total facular area (FA-T), the northern hemisphere's facular area (FA-N), the southern hemisphere's facular area (FA-S), the difference between northern and southern facular areas (FA-NS).

axis always perpendicular to the geomagnetic-dipole axis, GSE has the y-axis in the ecliptic plane pointing toward dusk, independent of the geomagnetic-dipole position (e.g. Laundal and Richmond, 2016). The total IMF field intensity $[B]$ is also analyzed. Most of the data sets were obtained from the NASA/GSFC's LRO OMNI data set. All 27-day averages are calculated over the daily averages (see Figure 2). More details can be found at omniweb.gsfc.nasa.gov/html/ow_data.html#1.

2.3. Ground Geomagnetic Activity Indices (GAI) and Newell's Coupling Function (NLL)

GAI-indices used are PCN (polar cap north), AE, AU, AL, Dst, Kp10, and Ap.

The Polar Cap North (PCN) one-minute index aims at characterizing the magnetic activity in the North polar cap that is driven by the IMF B_z-component. It is deduced from the deviations in the horizontal H and D magnetic-field components from the quiet level at the Qaanaaq (formerly known as Thule, Greenland) polar cap station.

AE, AU, and AL one-minute indices monitor the magnetic signature of the auroral electrojets in the Northern hemisphere. The magnetograms of the horizontal components from the 12 AE stations (> 56.5 °N) are superimposed on plots against UT. The AE-index at any epoch is defined by the separation between the upper (AU) and lower (AL) values at that epoch: $\mathrm{AE} = \mathrm{AU} - \mathrm{AL}$ (Davis and Sugiura, 1966). The AU- and AL-indices are intended to express the strongest current intensity of the eastward and westward auroral electrojets, respectively. The AE-index represents the overall activity of the electrojets (Menvielle et al., 2011).

The disturbance field (Dst) is the storm-time decrease in H, measured at the Earth's surface as a result of geomagnetic activity. The Dst-index is linearly dependent on the amplitude of the geomagnetic perturbation and is derived from hourly values of the horizontal geomagnetic component (H) obtained at four magnetic observatories at low and mid-latitudes

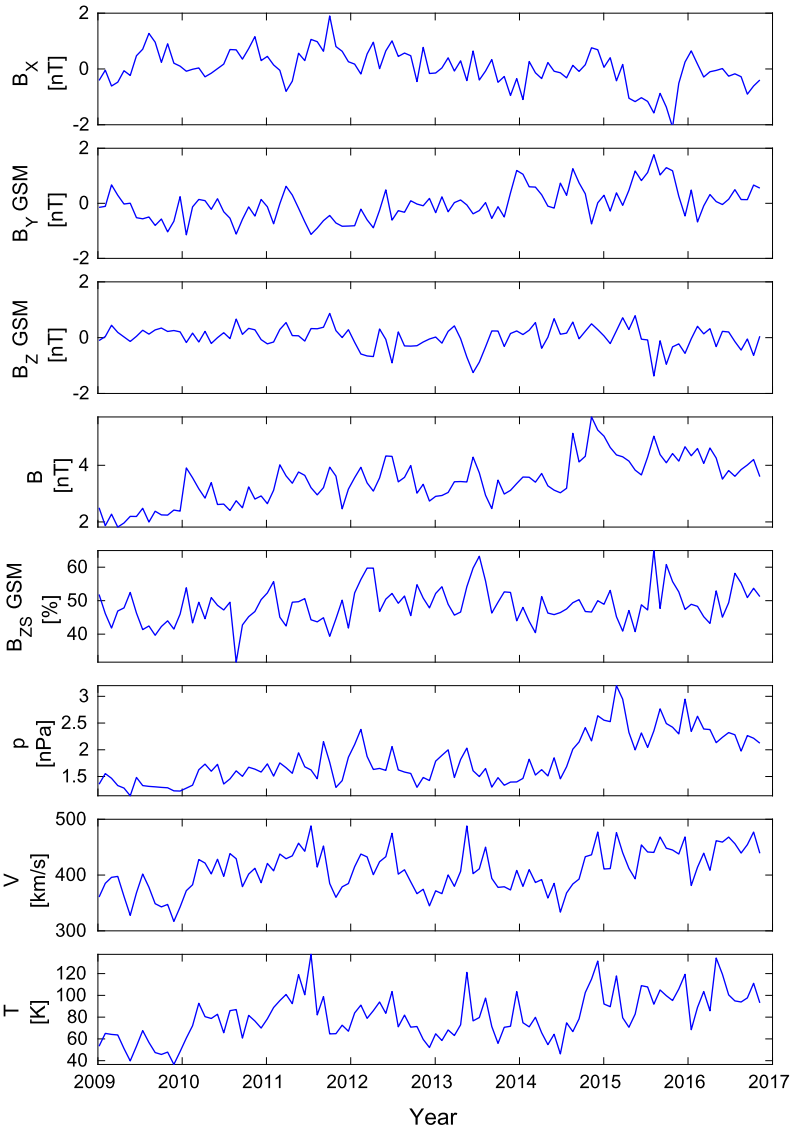

Figure 2 Time series of 27-day-averaged interplanetary magnetic-field components and solar-wind parameters (IMF and SWP).

and distributed evenly in longitude: Honolulu (Hawaii), San Juan (Puerto Rico), Hermanus (South Africa), and Kakioka (Japan) (see Sugiura, 1964; Mayaud, 1980).

The K-index is related quasi-logarithmically to the geomagnetic-disturbance amplitude measured for the horizontal component at a particular observatory, during a three-hour interval and after the quiet daily variation has been removed. The planetary K-index (Kp) is the weighted average of the local standardized K-indices of 13 geomagnetic observatories between 44° and 63° northern and southern geomagnetic latitudes. The three-hour Kp-index ranges in a scale from 0 (quiet) to 9 (greatly disturbed). The Kp10 is Kp multiplied by 10,

and in the low resolution OMNI (LRO) data set the Kp10 average is rounded to its nearest integer (i.e. 10, 13, 17, 20, ...).

To calculate the daily average level of geomagnetic activity, the Kp-scale must be converted back into an equivalent linear three-hour scale called Ap-index, dividing by two the amplitude range corresponding to each Kp. The Ap-index is calculated as the arithmetic average of eight three-hour averaged Ap-indices of a day. Sources: isgi.unistra.fr/indices_kp.php and ngdc.noaa.gov/stp/geomag/kp_ap.html.

Newell et al. (2007) derived a nearly universal coupling function that represents the rate of magnetic flux removed from the dayside magnetopause [$\mathrm{d}\Phi_{MP}/\mathrm{d}t$] that is itself an electric field. The rate at which magnetic flux is opened at the magnetopause is calculated as a function of the rate at which field lines approach the magnetopause (determined by the solar-wind velocity V). Additionally, they compute the fraction of field lines that merge at magnetosphere (calculated by a sine function of clock angle θ_c) and the strength of the transverse IMF (B_t, which is proportional to the amount of flux opened).

In this work we used a version of Newell's function derived by Tsyganenko and Andreeva (2015), which introduces a normalization factor of 10^{-4}, and we denote the merging function as the NLL-index:

$$\mathrm{NLL} = 10^{-4}\ V^{4/3}\ B_t^{2/3}\ \sin^{8/3}(\frac{\theta_c}{2}) \tag{1}$$

with V in $\mathrm{km\,s^{-1}}$ and B_t in nT, where $B_t = \sqrt{B_z^2 + B_y^2}$ is the IMF field component perpendicular to the Sun–Earth axis. Tsyganenko and Andreeva (2015) computed the NLL-index for each 5-minute average data record as an average over the 30-minute long trailing interval, immediately preceding the current moment. We binned the 5-minute data to 27-day resolution in order to compare with the other parameters.

Some of these parameters are displayed in Figure 3.

2.4. B_{zs}- and T-Indices

Two other types of parameters were tested in this work, as proxies of the interconnection between IMF and geomagnetic activity (B_{zs}) and of the imprint of particular magnetospheric current systems into the observed activity on surface (TI).

As is known (e.g. Schwenn, 2006), the southward IMF B_z is favorable to the energy transport from the SW into the Earth's magnetosphere. The daily percentage of the southward component of IMF, hereafter B_{zs}, was calculated from hourly values of IMF B_z in the GSM coordinate system. For day j:

$$B_{zs}^j = \frac{100\, n^j}{24} \tag{2}$$

where n^j is the number of IMF B_z GSM negative (southward) hourly means on day j. Then we averaged the daily B_{zs} over every 27-day period.

The T-indices were calculated using the x-component of separate contributions from magnetospheric currents on the Earth's surface, from TS05 model simulations. Namely, the x-component of the tail current sheet (T-TAIL), the symmetric ring current (T-SRC), the partial ring current (T-PRC), and the field-aligned currents (T-FAC). In order to compute T-indices, first all differences between the maximum and minimum (range) values of the

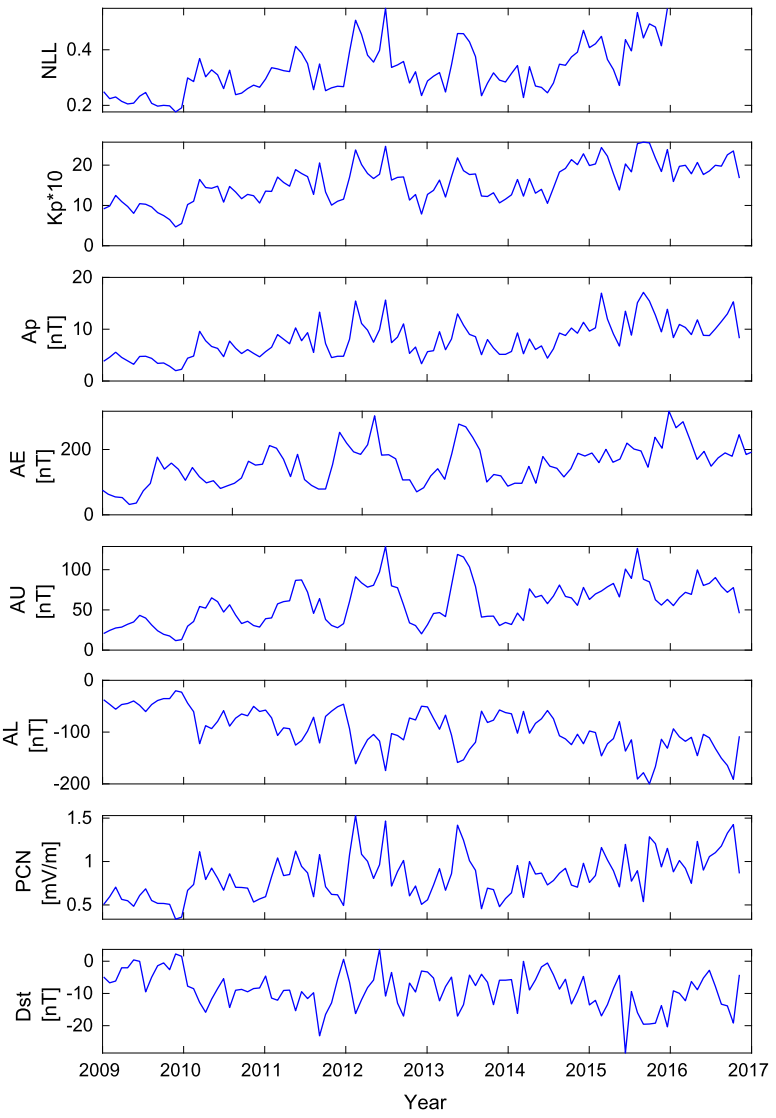

Figure 3 Time series of 27-day-averaged geomagnetic-activity indices (GAIs) and coupling function NLL.

corresponding x-component over each three-hour time interval were calculated, in nT, a total of eight values per day:

$$\Delta T8^{\mathrm{obs}}_{\mathrm{cur}}(i) = \max[T^{i}_{\mathrm{cur}},\ T^{i+1}_{\mathrm{cur}},\ T^{i+2}_{\mathrm{cur}}] - \min[T^{i}_{\mathrm{cur}},\ T^{i+1}_{\mathrm{cur}},\ T^{i+2}_{\mathrm{cur}}] \tag{3}$$

with $i = 1$, 4, 7, 10, 13, 16, 19, and 22. T^{i}_{cur} are hourly values of T_{cur} for hour i. The superscript "obs" stands for a certain observatory (COI, PAG, NVS, and BOU) and the subscript "cur" stand for a certain current system (TAIL, SRC, PRC, or FAC). Then, for each observatory, we computed an averaged daily value as the mean of each group of three-hour

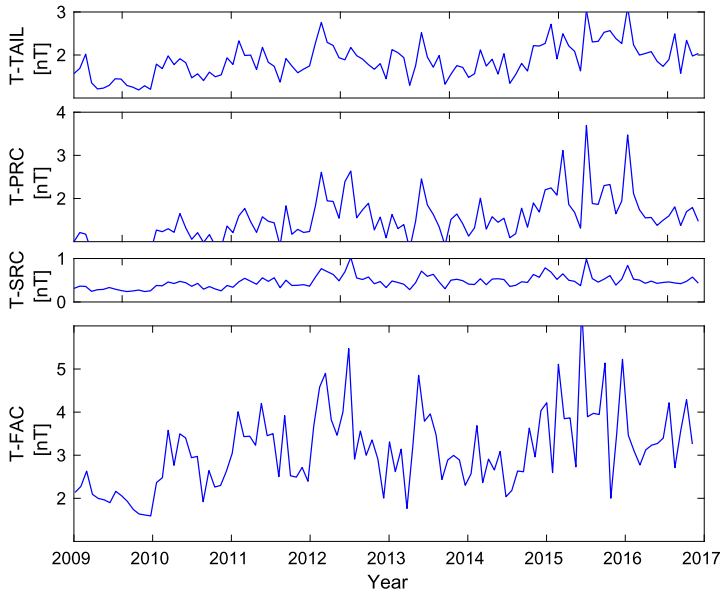

Figure 4 Time series of 27-day-averaged TI magnetospheric indices.

values:

$$T_{\mathrm{cur}}^{\mathrm{obs},j} = \frac{1}{8}\left(\Delta T8_{\mathrm{cur}}^{\mathrm{obs}}(1) + \Delta T8_{\mathrm{cur}}^{\mathrm{obs}}(4) + \cdots + \Delta T8_{\mathrm{cur}}^{\mathrm{obs}}(22)\right). \tag{4}$$

As a third step, we calculated a global daily mean, representative of the behavior seen at (northern hemisphere) mid-latitudes, using the corresponding daily $T_{\mathrm{cur}}^{\mathrm{obs},j}$ at all four observatories:

$$T_{\mathrm{cur}}^{j} = \frac{1}{4}\left(T_{\mathrm{cur}}^{\mathrm{COI},j} + T_{\mathrm{cur}}^{\mathrm{PAG},j} + T_{\mathrm{cur}}^{\mathrm{NVS},j} + T_{\mathrm{cur}}^{\mathrm{BOU},j}\right). \tag{5}$$

Finally, we averaged mid-latitude daily values over 27-day periods. TI-series are shown in Figure 4.

2.5. Toward–Away Asymmetries

The orientation of the IMF in the plane perpendicular to the z-axis of the Geocentric Solar Equatorial (GSEq) coordinate system (toward or away from the Sun), is known to also have an impact on geomagnetic activity (e.g. Sabbah, 1995; Zhao and Zong, 2012). Considering that the IMF is along the Parker spiral direction, there are two possible polarities, either "away" or "toward" (the Sun). The "away" (or positive) polarity implies IMF $B_y > 0$ in the GSEq coordinate system, while the "toward" (or negative) polarity implies IMF $B_y < 0$. The IMF polarity close to Earth changes as the Earth crosses the Heliospheric Current Sheet (HCS). To the North of the HCS, the polarity is the same as the solar magnetic polarity which has an oscillating cycle of 22 years. To address the possible influence of IMF polarity on geomagnetic activity, values of "toward–away" asymmetries were calculated for each of the analyzed parameters (see Sections 2.1 – 2.4).

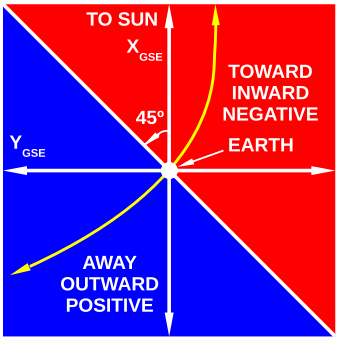

Figure 5 Definition of away and toward polarity seen from the Earth. Angles in $[45°, 225°]$ are considered away (outward) or positive polarity. Other angles are considered toward (inward) or negative polarity (Sabbah, 1995). Yellow arrows represent the IMF's trajectory and direction in the azimuthal GSE framework.

The Wilcox Solar Observatory (WSO: wso.stanford.edu/SB/SB.html) provides a list of well defined sector boundaries around the Sun inside which the IMF has positive or negative polarities, and such that: i) data are of good quality, ii) the reversal takes place cleanly, and iii) intervals on either side of the boundary have an uniform field direction for $\approx$4 days. The list is inferred from geomagnetic and spacecraft observations. This WSO boundary list was used to separate days with different polarity signs. When no data were available in the WSO list, "toward" and "away" polarities were calculated using the angle between the IMF GSE radial component ($\sqrt{B_x^2 + B_y^2}$) and the positive x GSE axis measuring the angle anti-clockwise and using daily means of IMF B_x and IMF B_y in the GSE coordinate frame, from NASA/GSFC's OMNI data set through OMNIWeb (see Figure 5) and Sabbah (1995) definition: IMF is "away" from the Sun when the angle is between 45° and 225° and is "toward" to the Sun in any other case. Note that the angle between B_y GSE and B_y GSEq in the two coordinate systems is small, $\approx 7°$, so they are sometimes used interchangeably.

Figure 6 shows our pixel plot of "toward" and "away" days from 2009 to 2016, obtained using the Wilcox Solar Observatory list of sector boundaries combined with calculation of toward and away days using the Sabbah (1995) criteria. From January 2009 to March 2012 the solar magnetic field has negative polarity (44 Bartels rotations); then, from April 2012 to March 2015 there is a transition period (40 rotations), and, finally, from April 2015 to 2016 the solar magnetic field has positive polarity (24 rotations). The Sun's North (South) Pole is most inclined toward the Earth in September (March), therefore, the dominant polarity seen by the Earth around September is that of the Sun (and the opposite around March).

The "toward–away" asymmetries (with respect to IMF polarity) of the 33 parameters were computed as follows. For each parameter mentioned in Sections 2.1 – 2.4, we split values into two groups and calculate separate averages for days when the IMF is directed toward the Sun (T), and days when the IMF is directed away from the Sun (W), and computed the two values:

$$\overline{T} = \frac{1}{n}\sum_{i=1}^{n} T^i, \qquad \overline{W} = \frac{1}{m}\sum_{i=1}^{m} W^i, \tag{6}$$

where $\overline{T}$ and $\overline{W}$ are mean values of a certain parameter over a Bartels rotation period, counting only "toward" days in the former case (in a total of n) and only "away" days in the latter case (in a total of m). Then, for each parameter, we obtained the asymmetry A over each Bartels period as the difference between the corresponding "toward" and "away" means:

$$A = \overline{T} - \overline{W}. \tag{7}$$

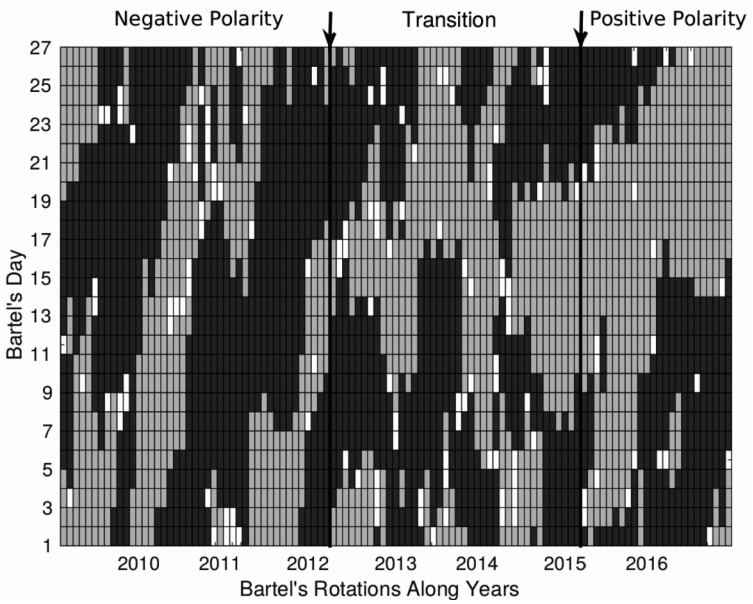

Figure 6 Days with toward/negative polarity (dark gray) and away/positive polarity (light gray) IMF. White days means missing data or polarity that could not be determined. Each column is a solar rotation (27 days) in the period 2009 – 2016. The solar magnetic field has negative polarity in 2009 – 2012 and has positive polarity in 2015 – 2016. The interval 2012 – 2015 is a transition period.

The standard error for each A was calculated as

$$\sigma_A = \sqrt{\frac{\sigma_T^2}{n} + \frac{\sigma_W^2}{m}} \tag{8}$$

where σ_T is the standard deviation of parameter values during "toward" days, and σ_W is the standard deviation of parameter values during "away" days. Asymmetries were standardized ($A^s = A/\sigma_A$).

Figure 7 shows an example of A asymmetries for B_z GSM, the Newell coupling function, the T-FAC index, and different GAI parameters. Note that A for B_z GSM and Dst was multiplied by -1 to facilitate the comparison. The percentage of toward-the-Sun days in each Bartels rotation is also shown, at the top-left of the figure.

3. Results and Discussion

In this section we present a correlation analysis of all the solar, solar-wind, and geomagnetic-field parameters and their asymmetries. Spearman's cross-correlation coefficients were calculated for the 27-day means for the 2009 – 2016 time interval, except in the case of Newell's coupling function, available only until 2015.

3.1. Correlation Analysis of 27-Day-Averaged Series

Spearman's cross-correlation coefficients r_S between the 33 parameters, averaged over 27-day intervals, were computed in order to search for a pattern that explains the physical

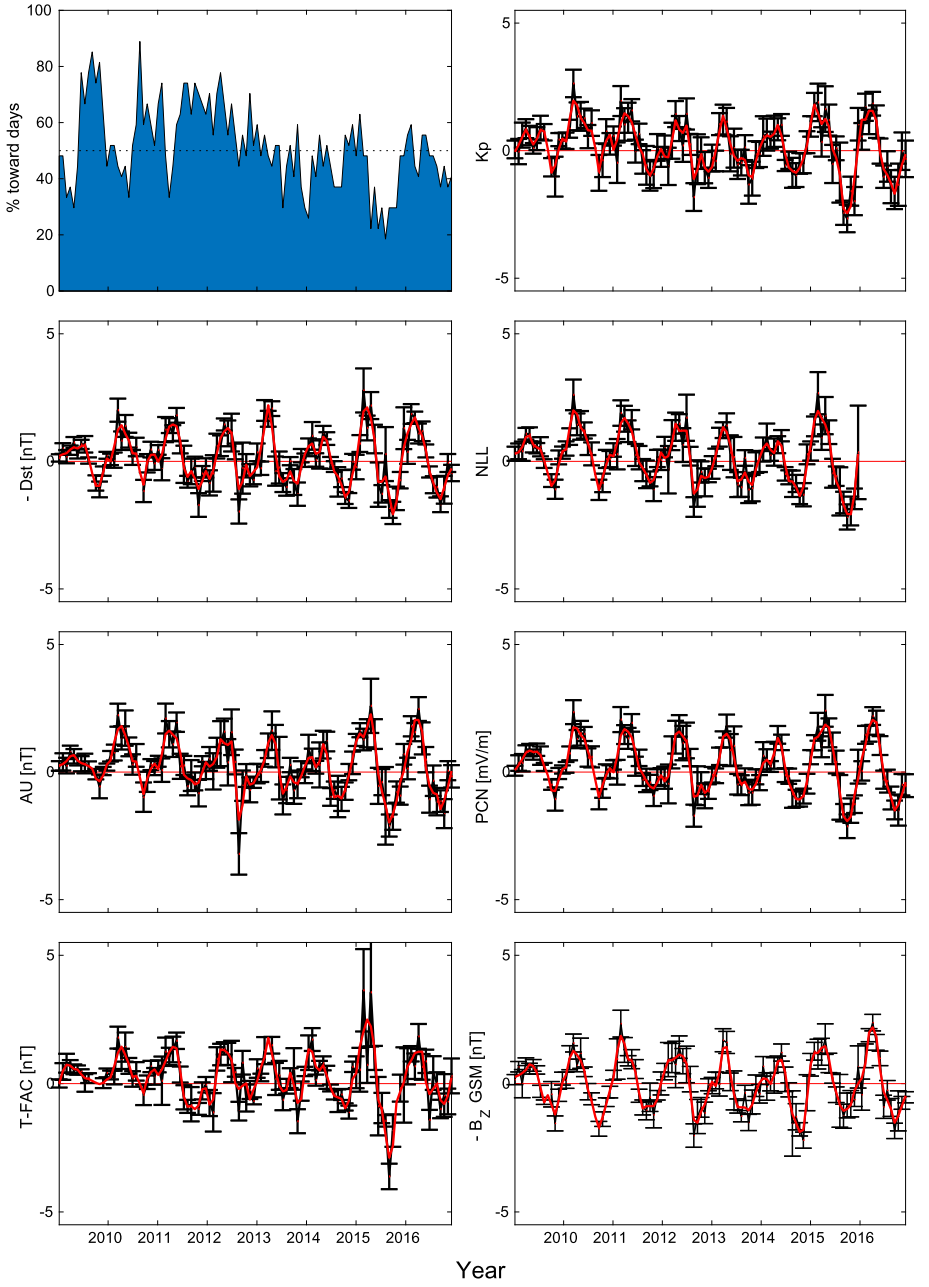

Figure 7 Top-left: Percentage of days with toward IMF during each Bartels rotation for the whole 2009 – 2016 period. Top-right: Time series of the asymmetry A for the Kp-index. From top to bottom, left to right: time series of A for the $-$Dst, the coupling function NLL, AU, PCN, T-FAC, and $-B_z$ GSM, with corresponding error bars. The smooth-red curves represent a LOESS regression model, using span $= 0.5$ (fraction of data used with the fitting procedure).

Table 3 Spearman's cross-correlation coefficients of solar parameters (in Bartels means) with $|r_s| \geq 0.4$ and $p \leq 0.05$.

Parameter	FA-T	FA-N	FA-S	SN-T	SN-N	SN-S	FA-NS	SN-NS	$F_{10.7}$
FA-T		0.77	0.89	0.84	0.59	0.83			0.90
FA-N	0.77		0.47	0.63	0.73	0.49	0.49		0.67
FA-S	0.89	0.47		0.82	0.45	0.90	−0.51	−0.50	0.86
SN-T	0.84	0.63	0.82		0.73	0.92			0.96
SN-N	0.59	0.73	0.45	0.73		0.49			0.66
SN-S	0.83	0.49	0.90	0.92	0.49			−0.56	0.91
FA-NS		0.49	−0.51					0.71	
SN-NS			−0.50			−0.56	0.71		
$F_{10.7}$	0.90	0.67	0.86	0.96	0.66	0.91			
B_x									
B_y GSE									
B_z GSE									
B_y GSM									
B_z GSM									
B	0.59	0.55	0.53			0.41			0.47
B_{zs} GSE									
B_{zs} GSM									
T									
ρ									
V									
p	0.42	0.54							
NLL	0.46	0.45	0.48			0.44			0.40
Kp	0.40	0.42	0.42						
Ap		0.41	0.40						
AE			0.43						
AU			0.42						
AL			−0.41						
PC									
Dst									
T-TAIL		0.46							
T-SRC	0.53	0.47	0.54	0.48		0.53			0.53
T-PRC	0.52	0.51	0.50	0.41		0.45			0.48
T-FAC									
Sum of absolute values	7.73	8.06	9.54	5.78	3.64	6.93	1.70	1.77	6.84
Number of correlations	12	15	17	8	6	11	3	3	10

processes involved in the solar-wind–magnetosphere coupling. Tables 3, 4, and 5 show the correlations obtained. As a criterion for choosing the "best" correlations, only values $|r_S| \geq 0.4$ and p-value ≤ 0.05 are shown.

Table 4 Spearman's cross-correlation coefficients of interplanetary medium parameters (in Bartels means) with $|r_s| \geq 0.4$ and $p \leq 0.05$.

Parameter	B_x	B_y GSE	B_z GSE	B_y GSM	B_z GSM	B	B_{zs} GSE	B_{zs} GSM	T	ρ	V	p
FA-T						0.59						0.42
FA-N						0.55						0.54
FA-S						0.53						
SN-T												
SN-N												
SN-S						0.41						
FA-NS												
SN-NS												
$F_{10.7}$						0.47						
B_x		−0.71		−0.70								
B_y GSE	−0.71			0.99								
B_z GSE					0.81		−0.81	−0.58				
B_y GSM	−0.70	0.99										
B_z GSM			0.81				−0.69	−0.82				
B									0.60		0.54	0.75
B_{zs} GSE			−0.81		−0.69			0.71				
B_{zs} GSM			−0.58		−0.82		0.71					
T						0.60					0.92	0.68
ρ												0.51
V						0.54			0.92			0.71
p						0.75			0.68	0.51	0.71	
NLL					−0.50	0.79		0.58	0.78		0.78	0.76
Kp						0.79		0.41	0.80		0.84	0.88
Ap						0.77			0.75		0.80	0.83
AE						0.74		0.46	0.74		0.79	0.74
AU						0.66		0.41	0.66		0.71	0.67
AL					0.41	−0.75		−0.46	−0.76		−0.80	−0.76
PC						0.63		0.43	0.64		0.71	0.67
Dst						−0.50			−0.54		−0.58	−0.50
T-TAIL						0.65		0.42	0.62		0.64	0.79
T-SRC						0.67		0.43	0.59		0.56	0.61
T-PRC						0.77		0.45	0.60		0.60	0.75
T-FAC						0.57		0.46	0.68		0.72	0.64
Sum of absolute values	1.41	1.70	2.20	1.69	3.22	12.75	2.21	6.61	10.35	0.51	10.70	12.20
Number of correlations	2	2	3	2	5	20	3	13	15	1	15	18

Table 5 Spearman's cross-correlation coefficients of geomagnetic activity proxies (in Bartels means) with $|r_s| \geq 0.4$ and $p \leq 0.05$.

Parameter	NLL	Kp	Ap	AE	AU	AL	PC	Dst	T-TAIL	T-SRC	T-PRC	T-FAC
FA-T	0.46	0.40								0.53	0.52	
FA-N	0.45	0.42	0.41						0.46	0.47	0.51	
FA-S	0.48	0.42	0.40	0.43	0.42	−0.41				0.54	0.50	
SN-T										0.48	0.41	
SN-N												
SN-S	0.44									0.53	0.45	
FA-NS												
SN-NS												
$F_{10.7}$	0.40									0.53	0.48	
B_x												
B_y GSE												
B_z GSE												
B_y GSM												
B_z GSM	−0.50					0.41						
B	0.79	0.79	0.77	0.74	0.66	−0.75	0.63	−0.50	0.65	0.67	0.77	0.57
B_{zs} GSE												
B_{zs} GSM	0.58	0.41		0.46	0.41	−0.46	0.43		0.42	0.43	0.45	0.46
T	0.78	0.80	0.75	0.74	0.66	−0.76	0.64	−0.54	0.62	0.59	0.60	0.68
ρ												
V	0.78	0.84	0.80	0.79	0.71	−0.80	0.71	−0.58	0.64	0.56	0.60	0.72
p	0.76	0.88	0.83	0.74	0.67	−0.76	0.67	−0.50	0.79	0.61	0.75	0.64
NLL		0.93	0.92	0.91	0.82	−0.93	0.82	−0.64	0.84	0.87	0.90	0.85
Kp	0.93		0.97	0.94	0.85	−0.95	0.83	−0.63	0.80	0.77	0.84	0.79
Ap	0.92	0.97		0.93	0.82	−0.96	0.86	−0.70	0.78	0.79	0.86	0.80
AE	0.91	0.94	0.93		0.95	−0.98	0.87	−0.57	0.71	0.76	0.80	0.79
AU	0.82	0.85	0.82	0.95		−0.88	0.79		0.60	0.71	0.72	0.73
AL	−0.93	−0.95	−0.96	−0.98	−0.88		−0.88	0.64	−0.74	−0.77	−0.81	−0.80
PC	0.82	0.83	0.86	0.87	0.79	−0.88		−0.59	0.67	0.71	0.73	0.74
Dst	−0.64	−0.63	−0.70	−0.57		0.64	−0.59		−0.57	−0.51	−0.58	−0.54
T-TAIL	0.84	0.80	0.78	0.71	0.60	−0.74	0.67	−0.57		0.77	0.87	0.82
T-SRC	0.87	0.77	0.79	0.76	0.71	−0.77	0.71	−0.51	0.77		0.92	0.85
T-PRC	0.90	0.84	0.86	0.80	0.72	−0.81	0.73	−0.58	0.87	0.92		0.85
T-FAC	0.85	0.79	0.80	0.79	0.73	−0.80	0.74	−0.54	0.82	0.85	0.85	
Sum of absolute values	15.84	14.25	13.36	13.10	11.40	13.69	11.58	8.08	11.74	14.36	14.92	11.64
Number of correlations	22	19	17	17	16	18	16	14	17	22	22	16

FA-N and FA-S are the solar parameters with highest (in absolute value) correlation coefficients with parameters of other groups, and represent the activity in the Sun's chromosphere. They give us a valuable picture of the solar dynamo, vital in understanding the global structure of the Heliospheric Magnetic Field. At solar minimum (near 2009), the Sun has few facular areas (but never zero facular area, as can be seen from Figure 1), corresponding with a mostly dipolar magnetic field, with a slow wind at the solar equator and a fast wind at the poles. At maximum of activity (around 2014), the Sun has larger facular areas, with a multipolar magnetic field and a bi-modal wind distribution at all latitudes (Perri et al., 2018). FA-S is the solar parameter that has more significant correlations with other parameters.

Among the solar-wind parameters, the 27-day mean of the B-field is the parameter that has more significant correlations and the highest sum of absolute values of correlation coefficients, as can be seen at the bottom of Table 4.

The B_{zs} GSM, a 27-day average of the percentage of southward B_z GSM occurrences, correlates with GAI and TI parameters better than the 27-day-averaged B_z GSM. In fact, at this temporal resolution, correlations of B_z GSM with most GAI and TI parameters are less than 0.4. This shows that, in spite of the recurrent use of B_z GSM as a proxy for geomagnetic storms (with a timescale much shorter than the one resolved here), B_{zs} GSM is a better proxy of magnetospheric activity than B_z GSM, at the 27-day temporal resolution.

NLL is the combination of SW speed and IMF components which, among similar combinations, most closely represents the solar-wind–magnetospheric coupling (Newell et al., 2007). It shows significant correlations with all the other parameters, in Table 5.

Among GAI parameters, Kp presents the highest (and significant) correlation values. Finally, regarding T-indices, T-SRC and T-PRC have the highest (in absolute value) correlation coefficients with parameters from other groups. They represent the variations in the symmetric and the partial ring currents, respectively, due to energetic particles injected by solar-wind disturbances, i.e. ICMEs.

T-PRC and T-SRC associate the ring-current activity to chromospheric and photospheric activity, better than GAI parameters. Note in particular that Dst, a standard ring-current index, has no significant correlations with solar parameters. Also, Dst shows lower correlations with B and the coupling function NLL than T-SRC and T-PRC indices.

Comparing the trends of these parameters is of particular interest for identification of causal relationships between solar and terrestrial phenomena.

3.2. Analysis of 27-Day-Mean Series of Asymmetries

One interesting result of the analysis of the asymmetry-parameter variations is the annual variation in 27-day asymmetries in the GAI parameters and NLL coupling function (see Figure 7), but also in B_{zs} GSM (not shown) and B_z GSM. Asymmetries for different parameters were computed as explained in Section 2.5. For NLL, AU, PCN, T-FAC, and Kp we see positive asymmetries at the first half of the year and negative at the second half, with maxima (minima) near the equinoxes and zero asymmetry near the solstices. We see the same for $-B_z$ GSM and $-$Dst, since these values have the opposite sign. It means that every year the values of these parameters are larger when IMF points toward (away) the Sun than the values when IMF points away (toward) the Sun in the first (second) half of the year. This agrees with Zhao and Zong (2012), who found that geomagnetic activity is much more intense around March equinox when the direction of IMF is toward the Sun, while much more intense around September equinox when the direction of IMF is away from the Sun.

These observations are in agreement with the Russell–McPherron (R–M) effect (Russell and McPherron, 1973) proposed to explain the semiannual variation of geomagnetic activity

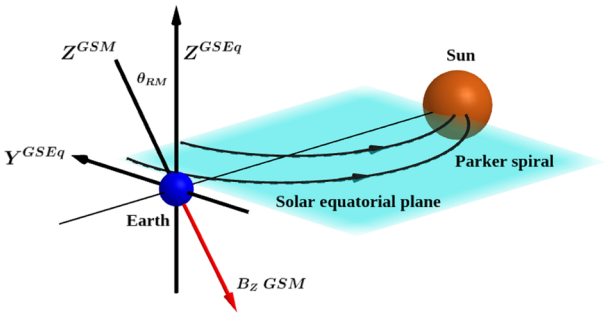

Figure 8 The θ_{RM} during the March equinox, with IMF toward the Sun. The B_z GSM southward (red vector) increases due to the contribution of the negative B_y GSEq. Figure adapted from Poblet, Azpilicueta, and Lam (2020).

(SAV). The IMF tends to be parallel to the solar wind flowing from the Sun, and as a result it lies mostly over the solar equatorial plane (x–y plane in the GSEq frame) (e.g. Koskinen, 2011). On the other hand, the probability of reconnection between the IMF and the Earth's field increases for larger values of the projection of IMF along -z GSM axis. In this context, Russell and McPherron (1973) suggested that the relevant parameter to measure the probability of geomagnetic activity could be the θ_{RM}-angle between z-GSM and z-GSEq axes: the larger θ_{RM}, the more the solar equatorial plane is tilted relative to the GSM magnetospheric equatorial plane, increasing the probability for reconnection. Both coordinate systems share the same x-axis (line pointing from the Earth to the Sun), and as a result θ_{RM} is measured in the y–z plane of both GSM and GSEq reference frames (see Figure 8).

The R–M mechanism could explain the observed SAV, since θ_{RM} attains larger (absolute) values close to the equinoxes (more exactly, beginning of April and October) (e.g. Lockwood et al., 2020). There are, nonetheless, two other mechanisms proposed to explain SAV (e.g. Poblet, Azpilicueta, and Lam, 2020; Lockwood et al., 2020): the axial hypothesis, which states the main cause is the position of the Earth with respect to the solar equator (the heliographic latitude), with maximum near the equinoxes ($\pm 7.5°$) and minimum near solstices ($\approx 0°$); the equinoctial hypothesis that identifies as the most relevant parameter the angle between the Earth–Sun line and the geomagnetic-dipole axis of the Earth (the tilt angle, or its complement).

Zhao and Zong (2012) noticed that if R–M is the dominant mechanism behind SAV, a toward/away asymmetry should be seen in geomagnetic activity. For the same θ_{RM}-angle, the IMF B_z-GSM projection can be positive or negative depending on the IMF polarity. As shown by them, during the September equinox when θ_{RM} attains lowest negative values ($\approx -26°$), the IMF B_z-GSM is negative for away IMF polarity and positive otherwise. During the March equinox (see Figure 8), when θ_{RM} attains the highest positive values ($\approx 26°$), the IMF B_z-GSM is negative for toward IMF polarity and positive otherwise. In this way, the dependence of magnetic-reconnection probability on the toward/away polarity, introduces an asymmetry between March and September equinoxes: during toward IMF polarity, the geomagnetic activity is maximum in March and minimum in September. An annual periodicity of this asymmetry should then be seen.

As is seen in the top-left of Figure 7 the days with toward IMF prevail in 2009 – 2012 and days with away IMF prevail in 2015 – 2016, coinciding with the polarity of Sun's northern hemisphere in both time intervals. This means that the Earth was located North of the heliospheric current sheet most of the time. It is the Earth's prevailing position since Solar Cycle 16 (Mursula and Hiltula, 2003).

We identify the annual oscillation in 27-day-mean values of the asymmetry for GAI parameters and for the NLL coupling function, as shown in Figure 7. The B_z-GSM and

Table 6 Spearman's correlation coefficients between Kp asymmetries and asymmetries of other parameters.

Parameter	Correlation coefficient
Ap	0.97
AE	0.93
AL	−0.92
AU	0.91
NLL	0.91
PC	0.89
Dst	−0.82
T-FAC	0.75
B_{zs} GSM	0.72
B_z GSM	−0.70
T-SRC	0.69
V	0.66
T-PRC	0.62
T	0.60
T-TAIL	0.59
p	0.50

B_{zs}-GSM parameters also show a similar oscillation. As Figure 7 shows, the asymmetry is always positive in March and negative in September. What we can also see is that the maxima in March show the highest values during the 2009 – 2012 period of solar negative polarity and the minima in September show the lowest values in the 2015 – 2016 period when the solar polarity is positive. This behavior can in principle be explained due to the R–M mechanism, although a larger data set, including several solar-polarity inversions, would be needed to draw a more robust conclusion.

In search for the ubiquitous presence (or not) of the annual oscillation in series of toward/away asymmetries, Table 6 shows the correlation between the Kp-asymmetry and the B_z GSM, the B_{zs} GSM, three solar-wind parameters, the NLL, the GAI, and the TI-indices asymmetries. When computing cross-correlations between different asymmetries and the Kp-asymmetry, we are evaluating the presence of a synchronized annual oscillation in all those different parameters' asymmetries, as the Kp-asymmetry is very closely fitted by a sine wave. The correlation is low with other IMF parameters and with solar parameters.

4. Conclusion

In order for the global dynamical state of the Sun to influence the Earth, some time should elapse. This study considers time averages over whole Bartels rotation periods (27 days), for different parameters involved in Sun–Earth interaction processes.

We computed hourly synthetic series of the x-component of four magnetospheric current systems at Earth's surface, in the 2009 – 2016 time period, using the TS05 model at the geomagnetic coordinates of four magnetic observatories in mid-latitudes (≈ 40 °N). Four new mid-latitude geomagnetic indices (T-indices) were derived from these series: T-TAIL (from tail current), T-SRC (symmetric ring current), T-PRC (partial ring current), and T-FAC (field-aligned current). Each T-index measures the contribution to the geomagnetic activity of its corresponding current field. The T-SRC and T-PRC indices have better correlations

with solar parameters than other geomagnetic-activity indices and solar-wind parameters. A relation between solar parameters and the ring-current system is inferred from these results. We also calculated the B_{zs} GSM, as the percentage of hourly occurrences of the southward B_z GSM in a day. It is a possible substitute for the most often used B_z GSM, as an estimator of the magnetospheric activity at the 27-day temporal resolution.

The geomagnetic activity observed during Solar Cycle 24 was largely driven by high-speed solar-wind streams (e.g. Richardson, Cliver, and Cane, 2002; Gerontidou, Mavromichalaki, and Daglis, 2018). As a result, strong correlations were expected between solar-wind temperature, speed, and ram pressure, and geomagnetic-activity indices such those tested here. Although those solar-wind parameters correlate strongly with GAI, they do not show as high correlations with solar-surface parameters as does the IMF B-intensity (see Table 4).

We analyzed the behavior of the working parameters with respect to the toward/away asymmetry, in search for some possible influence of the solar magnetic-field polarity over geomagnetic activity. We identified an annual oscillation in 27-day-mean values of geomagnetic activity indices and also Newell coupling function asymmetries, as shown in Figure 7. The B_z-GSM and B_{zs}-GSM parameters also show the same oscillation. We think this result favors the Russell–McPherron mechanism as the dominant mechanism explaining semiannual variation of geomagnetic activity.

The main conclusions derived from the analysis presented above, based on the correlation analysis of a large data set of parameters relating the different stages of Sun–Earth interaction processes, are the following:

i) Hemispheric facular areas computed as averages over 27-day periods show better correlations with solar-wind parameters (in particular the total IMF field B) and with geomagnetic-activity indices (in particular Kp) than other solar parameters such as the hemispheric sunspot numbers or the solar radio flux $F_{10.7}$. Furthermore, they evolve in a more continuous way along the solar cycle than sunspots, never getting to zero even at solar minimum.
ii) T-SRC and T-PRC indices are new parameters defined here to represent the dynamics of the ring current. They correlate better with solar parameters than the Dst-index, which is more frequently used as a proxy for the energy of the ring current. Newell's coupling function computed from solar-wind and IMF parameters, and the planetary index of global geomagnetic activity Kp, both show significant correlations with a large number of other proxies. Nonetheless, their correlation with solar-surface parameters is lower than what is obtained using the newly defined magnetospheric-activity proxies T-SRC and T-PRC.
iii) The B_{zs} GSM-index defined in this study seems to be a better choice than B_z GSM to characterize magnetospheric activity at the 27-day temporal resolution, since it shows higher correlations with all GAI parameters.
iv) The total field B averaged over 27 days is the solar-wind parameter that correlates the best with solar-surface parameters, in particular facular areas.
v) The annual oscillation found in series of toward/away asymmetry for the GAI parameters, NLL, and both B_z GSM and B_{zs} GSM parameters seems to support that the Russell–McPherron mechanism is the main mechanism explaining SAV.
vi) Further support for the idea of the R–M mechanism is the variation of amplitude of the toward/away asymmetry with the solar magnetic-field polarity, which is also retrieved in our results. Our results suggest that, for the analyzed 2009 – 2016 period, which covers the two different solar polarities, solar positive polarity leads to geomagnetic activity

more intense during the September equinox and negative polarity leads to geomagnetic activity more intense during the March equinox.

Finally, the new indices proposed here (T-indices and B_{zs} GSM) should be tested further in other solar cycles to strengthen their use as proxies of the Sun–Earth interactions. It would be particularly interesting to follow the changes and inter-correlations of all these parameters (in particular B, B_{zs} GSM, FA-N, FA-S, TI, and NLL) in the coming years of the new cycle and investigate the main physical mechanisms involved.

Supplementary Information The online version contains supplementary material available at https://doi.org/10.1007/s11207-021-01856-8.

Acknowledgements We are grateful to N. Tsyganenko for kindly answering our questions about his model and for making his codes easily available to the science community. We acknowledge the use of NASA/GSFC's Space Physics Data Facility's OMNIWeb service and OMNI data. We acknowledge Teresa Barata and her collaborators for their courtesy in sharing with us the plage data computed by them. CITEUC is funded by National Funds through FCT – Foundation for Science and Technology (Projects UID/00611/2020 and UIDP/00611/2020) and FEDER – European Regional Development Fund through COMPETE 2020 Operational Program Competitiveness and Internationalization (project: POCI-01-0145-FEDER-006922). J. Fernandes acknowledges funding from POCH and Portuguese FCT grant SFRH/BSAB/143060/2018 and from the project ReNATURE-Valuation of Endogenous Natural Resources in the Central Region (CENTRO-01-0145-FEDER-000007). Y. Castillo was supported by the Erasmus Mundus Action 2 Consortium AMIDILA, Lot 15 – strand 1, 2013-2588/001-001-EM Action 2 Partnerships. A.L. Morozova is supported by FCT – Foundation for Science and Technology, post-doc grant SFRH/BPD/74812/2010. F.J.G. Pinheiro was funded through project UID/Multi/00611/2013. This study also benefited from project MAGGIC: PTDC/CTA-GEO /31744/2017 funded by FCT.

Declarations

Disclosure of Potential Conflicts of Interest The authors declare that they have no conflicts of interest.

References

Ballester, J.L., Oliver, R., Carbonell, M.: 2005, The periodic behaviour of the North-South asymmetry of sunspot areas revisited. *Astron. Astrophys.* **431**, L5. DOI. ADS.

Barata, T., Carvalho, S., Dorotovic, I., Pinheiro, F.J.G., Garcia, A., Fernandes, J., Lourenco, A.M.: 2018, Software tool for automatic detection of solar plages in the Coimbra Observatory spectroheliograms. *Astron. Comput.* **24**, 70. DOI. ADS.

Beggan, C.D., Beamish, D., Richards, A., Kelly, G.S., Thomson, A.W.P.: 2013, Prediction of extreme geomagnetically induced currents in the UK high-voltage network. *Space Weather* **11**, 407. DOI. ADS.

Buonsanto, M.J.: 1999, Ionospheric storms – a review. *Space Sci. Rev.* **88**, 563. DOI. ADS.

Castillo, Y.S., Pais, M.A., Fernandes, J., Ribeiro, P., Morozova, A.L., Pinheiro, F.J.G.: 2017, Geomagnetic activity at Northern Hemisphere's mid-latitude ground stations: how much can be explained using TS05 model. *J. Atmos. Solar-Terr. Phys.* **165**, 38. DOI. ADS.

Davis, T.N., Sugiura, M.: 1966, Auroral electrojet activity index AE and its universal time variations. *J. Geophys. Res.* **71**, 785. DOI. ADS.

Dorotovič, I., Rybák, J., Garcia, A., Journoud, P.: 2010, North-south asymmetry of Ca II K regions determined from OAUC spectroheliograms: 1996 – 2006. In: Dorotovic, I. (ed.) *20th National Solar Physics Meeting* **20**, 58. ADS.

Georgieva, K., Kirov, B., Tonev, P., Guineva, V., Atanasov, D.: 2007, Long-term variations in the correlation between NAO and solar activity: the importance of north south solar activity asymmetry for atmospheric circulation. *Adv. Space Res.* **40**, 1152. DOI. ADS.

Gerontidou, M., Mavromichalaki, H., Daglis, T.: 2018, High-speed solar wind streams and geomagnetic storms during Solar Cycle 24. *Solar Phys.* **293**, 131. DOI. ADS.

Gonçalves, E., Mendes-Lopes, N., Dorotovič, I., Fernandes, J.M., Garcia, A.: 2014, North and South hemispheric solar activity for cycles 21 – 23: asymmetry and conditional volatility of plage region areas. *Solar Phys.* **289**, 2283. DOI. ADS.

Janardhan, P., Fujiki, K., Ingale, M., Bisoi, S.K., Rout, D.: 2018, Solar cycle 24: an unusual polar field reversal. *Astron. Astrophys.* **618**, A148. DOI. ADS.
Joshi, B., Bhattacharyya, R., Pandey, K.K., Kushwaha, U., Moon, Y.-J.: 2015, Evolutionary aspects and north-south asymmetry of soft X-ray flare index during solar cycles 21, 22, and 23. *Astron. Astrophys.* **582**, A4. DOI. ADS.
King, J.H., Papitashvili, N.E.: 2005, Solar wind spatial scales in and comparisons of hourly Wind and ACE plasma and magnetic field data. *J. Geophys. Res.* **110**, A02104. DOI. ADS.
Koskinen, H.: 2011, *Physics of Space Storms: From the Solar Surface to the Earth*, Springer, Berlin. ISBN 987-3-642-00310-3. DOI.
Laundal, K.M., Richmond, A.D.: 2016, Magnetic coordinate systems. *Space Sci. Rev.* **206**, 27. DOI. ADS.
Lekshmi, B., Nandy, D., Antia, H.M.: 2018, Asymmetry in solar torsional oscillation and the sunspot cycle. *Astrophys. J.* **861**, 121. DOI. ADS.
Lockwood, M., Owens, M.J., Barnard, L.A., Haines, C., Scott, C.J., McWilliams, K.A., Coxon, J.C.: 2020, Semi-annual, annual and Universal Time variations in the magnetosphere and in geomagnetic activity: 1. Geomagnetic data. *J. Space Weather Space Clim.* **10**, 23. DOI. ADS.
Mayaud, P.N.: 1980, *Derivation, Meaning, and Use of Geomagnetic Indices*. *Geophys. Mono. Ser.* **22**. American Geophysical Union, Washington DC. DOI. ADS.
Menvielle, M., Iyemori, T., Marchaudon, A., Nose, M.: 2011, Geomagnetic indices. In: Mandea, M., Korte, M. (eds.) *Geomagnetic Observations and Models*, Springer, Berlin, 183. ADS.
Mordvinov, A.V., Pevtsov, A.A., Bertello, L., Petrie, G.J.D.: 2016, The reversal of the Sun's magnetic field in cycle 24. *J. Solar-Terr. Phys.* **2**, 3. DOI. ADS.
Mursula, K., Hiltula, T.: 2003, Bashful ballerina: southward shifted heliospheric current sheet. *Geophys. Res. Lett.* **30**. ADS.
Nepomnyashchikh, A., Mandal, S., Banerjee, D., Kitchatinov, L.: 2019, Can the long-term hemispheric asymmetry of solar activity result from fluctuations in dynamo parameters? *Astron. Astrophys.* **625**, A37. DOI. ADS.
Newell, P.T., Sotirelis, T., Liou, K., Meng, C.-I., Rich, F.J.: 2007, A nearly universal solar wind-magnetosphere coupling function inferred from 10 magnetospheric state variables. *J. Geophys. Res.* **112**, A01206. DOI. ADS.
Norton, A.A., Gallagher, J.C.: 2009, Solar-cycle characteristics examined in separate hemispheres: phase, Gnevyshev gap, and length of minimum. *Solar Phys.* **261**, 193. DOI. ADS.
Perri, B., Brun, A.S., Réville, V., Strugarek, A.: 2018, Simulations of solar wind variations during an 11-year cycle and the influence of north-south asymmetry. *J. Plasma Phys.* **84**, 765840501. DOI. ADS.
Poblet, F.L., Azpilicueta, F., Lam, H.-L.: 2020, Semiannual variation of Pc5 ultra-low frequency (ULF) waves and relativistic electrons over two solar cycles of observations: comparison with predictions of the classical hypotheses. *Ann. Geophys.* **38**, 953. DOI. ADS.
Richardson, I.G., Cliver, E.W., Cane, H.V.: 2002, Long-term trends in interplanetary magnetic field strength and solar wind structure during the twentieth century. *J. Geophys. Res.* **107**, A10. DOI. ADS.
Russell, C.T., McPherron, R.L.: 1973, Semiannual variation of geomagnetic activity. *J. Geophys. Res.* **78**, 92. DOI. ADS.
Sabbah, I.: 1995, North-South asymmetry of the daily interplanetary magnetic field spiral during the period: 1965 – 1990. *Earth Moon Planets* **70**, 173. DOI. ADS.
Schrijver, C.J.: 2015, Understanding space weather to shield society: a global road map for 2015 – 2025 commissioned by COSPAR and ILWS. *Adv. Space Res.* **55**, 2745. DOI. ADS.
Schüssler, M., Cameron, R.H.: 2018, Origin of the hemispheric asymmetry of solar activity. *Astron. Astrophys.* **618**, A89. DOI. ADS.
Schwenn, R.: 2006, Space weather: the solar perspective. *Liv. Rev. Solar Phys.* **3**, 2. DOI. ADS.
Sugiura, M.: 1964, Hourly values of the equatorial Dst for IGY. *Ann. Int. Geophys. Year* **35**, 945.
Temmer, M., Veronig, A., Hanslmeier, A.: 2002, Hemispheric sunspot numbers Rn and Rs: catalogue and N-S asymmetry analysis. *Astron. Astrophys.* **390**, 707. DOI. ADS.
Temmer, M., Rybák, J., Bendík, P., Veronig, A., Vogler, F., Otruba, W., Pötzi, W., Hanslmeier, A.: 2006, Hemispheric sunspot numbers Rn and Rs from 1945 – 2004: catalogue and N-S asymmetry analysis for solar cycles 18 – 23. *Astron. Astrophys.* **447**, 735. DOI. ADS.
Thomson, A.W.P.: 2013, *Space Weather Applications of Geomagnetic Observatory Data* **3**, Real Instituto y Observatorio de la Armada.
Tsyganenko, N.A., Andreeva, V.A.: 2015, A forecasting model of the magnetosphere driven by an optimal solar wind coupling function. *J. Geophys. Res.* **120**, 8401. DOI. ADS.
Tsyganenko, N.A., Sitnov, M.I.: 2005, Modeling the dynamics of the inner magnetosphere during strong geomagnetic storms. *J. Geophys. Res.* **110**, A03208. DOI. ADS.
Waldmeier, M.: 1971, The asymmetry of solar activity in the years 1959 – 1969. *Solar Phys.* **20**, 332. DOI. ADS.

Zhao, H., Zong, Q.G.: 2012, Seasonal and diurnal variation of geomagnetic activity: Russell-McPherron effect during different IMF polarity and/or extreme solar wind conditions. *J. Geophys. Res.* **117**, A11222. DOI. ADS.

Authors and Affiliations

Yvelice Castillo[1,2,3] · Maria Alexandra Pais[2,3] · João Fernandes[2,4] · Paulo Ribeiro[2] · Anna L. Morozova[2] · Fernando J.G. Pinheiro[2]

✉ Y. Castillo
yvelice.castillo@unah.edu.hn

M.A. Pais
pais@fis.uc.pt

J. Fernandes
jmfernan@mat.uc.pt

P. Ribeiro
pribeiro@ci.uc.pt

A.L. Morozova
annamorozovauc@gmail.com

F.J.G. Pinheiro
fjgpinheiro.astro@gmail.com

1 National Autonomous University of Honduras, Department of Astronomy and Astrophysics, 11101 Tegucigalpa, Honduras

2 University of Coimbra, CITEUC, Geophysical and Astronomical Observatory, 3040-004 Coimbra, Portugal

3 University of Coimbra, Department of Physics, 3004-516 Coimbra, Portugal

4 University of Coimbra, Department of Mathematics, 3004-516 Coimbra, Portugal

Terms and Conditions

Springer Nature journal content, brought to you courtesy of Springer Nature Customer Service Center GmbH ("Springer Nature").

Springer Nature supports a reasonable amount of sharing of research papers by authors, subscribers and authorised users ("Users"), for small-scale personal, non-commercial use provided that all copyright, trade and service marks and other proprietary notices are maintained. By accessing, sharing, receiving or otherwise using the Springer Nature journal content you agree to these terms of use ("Terms"). For these purposes, Springer Nature considers academic use (by researchers and students) to be non-commercial.

These Terms are supplementary and will apply in addition to any applicable website terms and conditions, a relevant site licence or a personal subscription. These Terms will prevail over any conflict or ambiguity with regards to the relevant terms, a site licence or a personal subscription (to the extent of the conflict or ambiguity only). For Creative Commons-licensed articles, the terms of the Creative Commons license used will apply.

We collect and use personal data to provide access to the Springer Nature journal content. We may also use these personal data internally within ResearchGate and Springer Nature and as agreed share it, in an anonymised way, for purposes of tracking, analysis and reporting. We will not otherwise disclose your personal data outside the ResearchGate or the Springer Nature group of companies unless we have your permission as detailed in the Privacy Policy.

While Users may use the Springer Nature journal content for small scale, personal non-commercial use, it is important to note that Users may not:

1. use such content for the purpose of providing other users with access on a regular or large scale basis or as a means to circumvent access control;
2. use such content where to do so would be considered a criminal or statutory offence in any jurisdiction, or gives rise to civil liability, or is otherwise unlawful;
3. falsely or misleadingly imply or suggest endorsement, approval , sponsorship, or association unless explicitly agreed to by Springer Nature in writing;
4. use bots or other automated methods to access the content or redirect messages
5. override any security feature or exclusionary protocol; or
6. share the content in order to create substitute for Springer Nature products or services or a systematic database of Springer Nature journal content.

In line with the restriction against commercial use, Springer Nature does not permit the creation of a product or service that creates revenue, royalties, rent or income from our content or its inclusion as part of a paid for service or for other commercial gain. Springer Nature journal content cannot be used for inter-library loans and librarians may not upload Springer Nature journal content on a large scale into their, or any other, institutional repository.

These terms of use are reviewed regularly and may be amended at any time. Springer Nature is not obligated to publish any information or content on this website and may remove it or features or functionality at our sole discretion, at any time with or without notice. Springer Nature may revoke this licence to you at any time and remove access to any copies of the Springer Nature journal content which have been saved.

To the fullest extent permitted by law, Springer Nature makes no warranties, representations or guarantees to Users, either express or implied with respect to the Springer nature journal content and all parties disclaim and waive any implied warranties or warranties imposed by law, including merchantability or fitness for any particular purpose.

Please note that these rights do not automatically extend to content, data or other material published by Springer Nature that may be licensed from third parties.

If you would like to use or distribute our Springer Nature journal content to a wider audience or on a regular basis or in any other manner not expressly permitted by these Terms, please contact Springer Nature at

onlineservice@springernature.com